

**Multimetastability effect on the intermediate stage of phase separation in BaO-SiO<sub>2</sub> glass**Katsuaki Nakazawa <sup>1,\*</sup>, Yuhki Tsukada <sup>2</sup>, Shin-ichi Amma <sup>3</sup>, Kazutaka Mitsuishi <sup>4</sup>,  
Kiyou Shibata <sup>5</sup> and Teruyasu Mizoguchi <sup>5</sup><sup>1</sup>*International Center for Young Scientists (ICYS), National Institute for Materials Science, 1-2-1 Sengen, Tsukuba, Ibaraki 305-0047, Japan*<sup>2</sup>*Department of Materials Design Innovation Engineering, Graduate School of Engineering, Nagoya University, Furo-cho, Chikusa-ku, Nagoya, Aichi 464-8603, Japan*<sup>3</sup>*Materials Integration Laboratories, AGC Inc., 1-1 Suehiro-cho, Tsurumi-ku, Yokohama-shi, Kanagawa 230-0045, Japan*<sup>4</sup>*Research Center for Advanced Measurement and Characterization, National Institute for Materials Science, 1-2-1 Sengen, Tsukuba, Ibaraki 305-0047, Japan*<sup>5</sup>*Institute of Industrial Science, The University of Tokyo, Komaba, Meguro-ku, Tokyo 153-8505, Japan*

(Received 9 November 2021; revised 26 February 2022; accepted 15 June 2022; published 18 July 2022)

Controlling the phase separation phenomenon can enhance the properties of glass materials, such as transparency and strength. However, the initial and intermediate stages of phase separation of amorphous glass are yet to be understood completely. In this study, we performed an *in situ* observation on glass through scanning transmission electron microscopy, which possesses a high spatial resolution and chemical sensitivity. We visualized the phase-separated structure in the initial and intermediate stages of phase separation and observed a local and rapid change in the phase-separated structures and the formation of regions with advanced and delayed degrees of phase separation. The results were compared with the phase-field simulation and it was concluded that the characteristic change of the phase-separated structures is attributable to the multimetastability of the amorphous phase.

DOI: [10.1103/PhysRevResearch.4.033052](https://doi.org/10.1103/PhysRevResearch.4.033052)**I. INTRODUCTION**

Phase separation is a phenomenon that occurs when a uniform phase becomes unstable due to changes in temperature or pressure and separates into two stable phases [1]. This phenomenon can enhance the physical and chemical properties of glass [2] and is primarily studied in Fourier space through light [3], x-ray [4], or neutron [5] scattering methods. These studies have revealed the laws for developing average structure [3,6]. Cahn and Hilliard modeled phase separation using the Gibbs energy of the system and the composition gradient energy [7–11], and showed that phase separation proceeds to minimize the total energy. From the viewpoint of Gibbs energy, the phase separation type mainly can be classified into spinodal and binodal types, while the phase separation process can be divided into initial, intermediate, and final stages [1]. The initial stage begins with compositional fluctuation or nucleation, which becomes large in the intermediate stage and continues until the composition is binarized. After the composition is binarized, the phases begin coarsening in the final stage.

Amorphous glass materials have random and isotropic atomic structures [12]. The atomic structures of glass have multimetastable states that can undergo structural transitions (i.e., crystallization) [13], affecting the local phase-separated structure. The effect of the phase-separated structure on crystallization [14] and the cessation of the coarsening of the phase-separated structure have been reported [15]. Moreover, the effect on the local phase-separated structure when the transition occurs in the final stage has been relatively well studied [14–17]. However, the effect on the initial and intermediate stages has not been extensively researched and only a few observations of the phase-separated structure in the initial and intermediate stages have been made by imaging [18]. Because the phase-separated structure formation proceeds mainly during the initial and intermediate stages of the phase separation, it is essential to gain insight into these stages from the perspective of the phase separation process by imaging. Moreover, imaging the formation of the phase-separated structure is important to obtain guidelines for controlling the phase-separated structure and crystallization. The nanoscale sizes of the phases and the slight compositional differences between the phases in the initial and intermediate stages made it challenging to make observations through imaging. High resolution and chemical sensitivity are required for imaging the phase-separated structure at the initial and intermediate stages. Recently, our group revealed that the high-angle annular dark-field (HAADF) method conducted by scanning transmission electron microscopy (STEM) possesses sufficient spatial resolution and chemical sensitivity to observe the

\*NAKAZAWA.Katsuaki@nims.go.jp

Published by the American Physical Society under the terms of the [Creative Commons Attribution 4.0 International](https://creativecommons.org/licenses/by/4.0/) license. Further distribution of this work must maintain attribution to the author(s) and the published article's title, journal citation, and DOI.

phase-separated structure in the initial and intermediate stages [18,19].

Thus, the purpose of this study is to visualize the phase-separated structure in the initial and intermediate stages of the phase separation and to gain deep insight into the phase separation process of amorphous glass. We conducted an *in situ* STEM observation on the temporal change of local phase-separated structures using a microelectromechanical system (MEMS)-based heating holder. We examined the result of *in situ* STEM observation and compared them to the phase-field simulation. Therefore, temporal change of the phase-separated structure in the initial and intermediate stages was observed in real space. Additionally, a local and rapid change in the phase-separated structure being attributable to multimetastability of the amorphous phase was observed.

## II. MATERIALS AND METHODS

### A. Sample preparation

A silicate-based glass [27.0 BaO–73.0 SiO<sub>2</sub> (mol %)] was selected for the experiment with a glass transition temperature of 695 °C [20]. The bulk glass samples were prepared by the conventional melt-quench method. The mixed batch materials of SiO<sub>2</sub> and BaO were placed in a Pt<sub>90</sub>Rh<sub>10</sub> crucible and melted in an electric furnace at 1650 °C for 3 h in air. Subsequently, the obtained melt was quenched with water to produce small fragments, which were then mixed and remelted at 1680 °C for 3 h to homogenize the glass. The second melt was rapidly quenched by casting into two rollers with a cooling water flow to prevent the phase separation (referred to as a quenched sample from hereon). The flakes obtained from the quenching melt were transparent. Samples were thinned for the STEM observation by crushing in an agate mortar and then dispersed on Fusion E-chips (Protochips. Inc), a MEMS-based heating chip.

### B. STEM observation

The high-temperature STEM observations were performed using an aberration-corrected STEM (JEM-ARM200F, JEOL Ltd.). The compositional distribution was measured by HAADF image and image processing. The procedure of image processing is provided in the Supplemental Material [21]. The accelerating voltage was 200 kV, while the convergent semiangle, dwell time, and pixel size were set to 20.8 mrad, 8  $\mu$ s, and 0.38 nm  $\times$  0.38 nm, respectively. The number of scanning points for vertical and horizontal directions was 1024. The detection angle of HAADF was 54–220 mrad. We utilized a Fusion (Protochips. Inc.) system to perform an *in situ* heating experiment. The sample was heated at 695 °C for approximately 6.5 h which decomposed due to the binodal phase separation [22–25].

The composition and the thickness of the sample before and after heating were measured using a four-dimensional STEM (4DSTEM) equipped with a fast pixelated detector (4DCanvas, JEOL Ltd.) [26]. The composition of the sample was considered uniform before heating, while the thickness was measured. The composition and thickness of the sample were simultaneously measured after heating.

### C. Phase-field simulation

We considered a phase-field model for a virtual *A-B* binary system to conduct two-dimensional phase-field simulations of the microstructure evolution in the BaO–SiO<sub>2</sub> pseudobinary system, where the composition  $c_i(\mathbf{r}, t)$  ( $i = A, B$ ) was used as a field variable. The total free energy of the system ( $G_{\text{total}}$ ) was determined using Eq. (1).

$$G_{\text{total}} = \int_{\mathbf{r}} \left[ G_m + \frac{1}{2} \kappa \{ (\nabla c_A)^2 + (\nabla c_B)^2 \} \right] d\mathbf{r}, \quad (1)$$

where  $G_m$  is the Gibbs energy of the solution phase, and  $\kappa$  is the gradient energy coefficient. We considered regular solution and polynomial models for  $G_m$ .  $c_B$  is assigned to an independent variable, and its temporal evolution is obtained by solving the Cahn-Hilliard nonlinear diffusion equation [Eq. (2)],

$$\frac{\partial c_B(\mathbf{r}, t)}{\partial t} = \nabla M \nabla \frac{\delta G_{\text{total}}}{\delta c_B(\mathbf{r}, t)} + \xi(\mathbf{r}, t), \quad (2)$$

where  $M$  and  $\xi$  are the kinetic coefficient and thermal noise, respectively. We consider that  $M$  is given by  $M = M_c c_0 (1 - c_0)$ , where  $M_c$  is the temperature-dependent atomic mobility and  $c_0$  is the average composition. The Cahn-Hilliard equation was solved using the explicit finite-difference method. All physical parameters were reduced to dimensionless quantities in the numerical simulation using the following scaling factors: the product of the gas constant and absolute temperature,  $RT$ , for energy density; the unit grid size in the difference method,  $l_0$ , for length; and  $(M_c RT / l_0^2)^{-1}$  for time.

#### 1. Regular solution model

The regular solution model for the Gibbs energy  $G_m^{\text{reg}}$  is expressed in Eq. (3),

$$G_m^{\text{reg}} = c_A G_A + c_B G_B + RT (c_A \ln c_A + c_B \ln c_B) + c_A c_B \Omega, \quad (3)$$

where  $G_A$  and  $G_B$  are the Gibbs energies of the solution phase containing pure components *A* and *B*, respectively, and  $\Omega$  is the temperature-dependent interaction parameter. We considered  $G_A = G_B = 0$  for simplicity. We used a 256<sup>2</sup> uniform grid, and dimensionless parameters  $\hat{\Omega} = 3.007$  and  $\hat{\kappa} = 3.941$  in the numerical simulation. The average composition and dimensionless unit time step were set to  $c_0 = 0.2$  and  $\Delta \tau = 0.0005$ , respectively. The Gaussian distributed random numbers with mean zero and variance  $\sigma^2 = 0.032^2$  were used to incorporate the dimensionless noise term  $\hat{\xi}$  [27].

The simulation was initiated by seeding several minor phases with  $c_B = 0.93$  in a matrix phase with  $c_B = 0.15$ . We combined the microstructures simulated for  $\tau = 250$  (lower left side) and  $\tau = 10$  (upper right side) to simulate the microstructure evolution when its domains with different degrees of the phase separation progress coexisted. Subsequently, we restarted the phase-field simulation using the combined microstructure.

## 2. Polynomial model

The polynomial model for the Gibbs energy  $G_m^{\text{poly}}$  is expressed in Eq. (4),

$$G_m^{\text{poly}} = a(c_B - 0.04)^2(c_B - 0.25)^2(c_B - 0.5)^2(c_B - 0.8)^2 \\ \times (c_B - 0.96)^2 + b(c_B - 0.04)^2(c_B - 0.6)^2 \\ \times (c_B - 0.96)^2 + c(c_B - 0.04)^2(c_B - 0.96)^2 \\ + d(c_B - 0.5)^2, \quad (4)$$

where  $a$ ,  $b$ ,  $c$ , and  $d$  are temperature-dependent coefficients. We used a  $128^2$  uniform grid and dimensionless parameters  $\hat{a} = 7417$ ,  $\hat{b} = 9.889$ ,  $\hat{c} = 2.472$ ,  $\hat{d} = 0.3090$ , and  $\hat{k} = 3.116$  in the numerical simulation. The average composition and dimensionless unit time step were set to  $c_0 = 0.35$  and  $\Delta\tau = 0.008$ , respectively. The Gaussian distributed random numbers with mean zero and variance  $\sigma^2 = 0.008^2$  were used to incorporate the dimensionless noise term  $\hat{\xi}$ .

The polynomial function derived Gibbs energy has several local minima at specific compositions. Because the average composition is within the spinodal region, phase separation by the spinodal decomposition occurs when the simulation is initiated from a homogeneous solution phase with a small compositional fluctuation. However, the simulation produced a metastable microstructure consisting of two phases with the compositions where the Gibbs energy has local minima. Thus, two different metastable phase-separated microstructure domains were combined in this study, and the subsequent microstructure evolution was simulated.

## III. RESULTS AND DISCUSSION

Based on the phase diagrams reported in previous studies [22,23,25], the silicate-based glass 27.0 BaO–73.0 SiO<sub>2</sub> (mol %) separated into major and minor phases of BaO (35.0 BaO–65.0 SiO<sub>2</sub>) and SiO<sub>2</sub> (0.0 BaO–100.0 SiO<sub>2</sub>) by binodal phase separation at 695 °C, respectively. The minor SiO<sub>2</sub> phase was almost pure with a volume fraction of 23%, resulting in the formation of a droplet structure. Figure 1 shows the thickness and composition maps of the sample measured by 4DSTEM before and after heating [26,28]. The sample has a uniform compositional distribution before heating. The zero value in the thickness map indicates the vacuum area; the thickness gradually increases from left to right. However, the compositional distribution becomes nonuniform after heating, with the appearance of spherical regions with a low BaO composition (blue color). The composition is in the range of 17–35 BaO mol %, which is narrower than that of the two-phase coexistence region (0–35 BaO mol %) [23]. According to the phase diagram of the previous report [23], SiO<sub>2</sub> phases with high purity should be precipitated. This discrepancy was attributed to the combination of the properties of STEM and the phase-separated structure. Because the obtained STEM image was a projection image, the information along the irradiation direction (thickness direction) was integrated or averaged. In this sample, the major BaO phases overlapped the minor SiO<sub>2</sub> phases, and the measured composition of the SiO<sub>2</sub> phases was averaged with the overlapping BaO phases. Thus, the measured BaO composition at the SiO<sub>2</sub> phases was overestimated. Thus, the blue color region in the compositional map indicates the area of the precipitated SiO<sub>2</sub> phases.

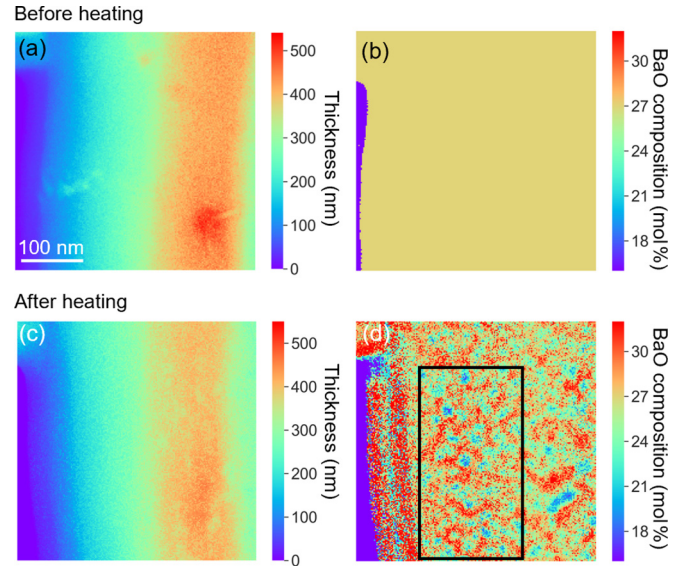


FIG. 1. (a) Thickness map and (b) composition map of the sample before heating. (c) Thickness map and (d) composition map of the sample after heating. The sample thickness increases from left to right in the image, while the composition becomes nonuniform after heating.

The region inside the black rectangle in Fig. 1(d) is selected for analyzing the temporal change in the compositional distribution. The time series of the compositional distribution in this region are shown in Figs. 2(a)–2(f); the red and blue colors correspond to the regions with high and low BaO compositions, respectively. There were temporal changes in the compositional distribution. For example, the size of the nucleated SiO<sub>2</sub> phase encircled by the dashed lines increased as time passed. The BaO compositions in the BaO and SiO<sub>2</sub> phases increased and decreased, respectively [Figs. 2(b)–2(f);  $t = 2, 130\text{--}23, 150$  s]. We defined the area where the SiO<sub>2</sub> phase precipitated to quantitatively measure the temporal changes of compositional distribution. The region whose BaO composition was lower than 25.8 BaO mol % and area larger than 9 pixels (20 nm<sup>2</sup>) was defined as the area where SiO<sub>2</sub> phases precipitated. Hereafter, for simplicity, we call the area where the SiO<sub>2</sub> phase precipitated as the SiO<sub>2</sub> phase. Additionally, the average compositions of the BaO and SiO<sub>2</sub> phases are defined as the top and bottom 10th percentile of BaO composition of all pixels, respectively. Since SiO<sub>2</sub> phases should be defined according to whether the BaO composition is lower than the average value, the threshold should be set to 27 mol % ideally. However, the HAADF image and the compositional image created based on the HAADF image are affected by noise. To reduce the effect of noise, a margin of about 5% was taken. Similarly, the composition of SiO<sub>2</sub> and BaO phases should be measured by their maximum values, but to reduce the effects of noise, they are defined as the top or bottom 10th percentile of the BaO composition of all pixels. We measured the temporal changes of average size and the number of the SiO<sub>2</sub> phases, and the average BaO compositions in the BaO and SiO<sub>2</sub> phases.

Figures 2(g) and 2(h) show the average BaO composition in the BaO and SiO<sub>2</sub> phases, respectively. Figures 2(i) and 2(j)

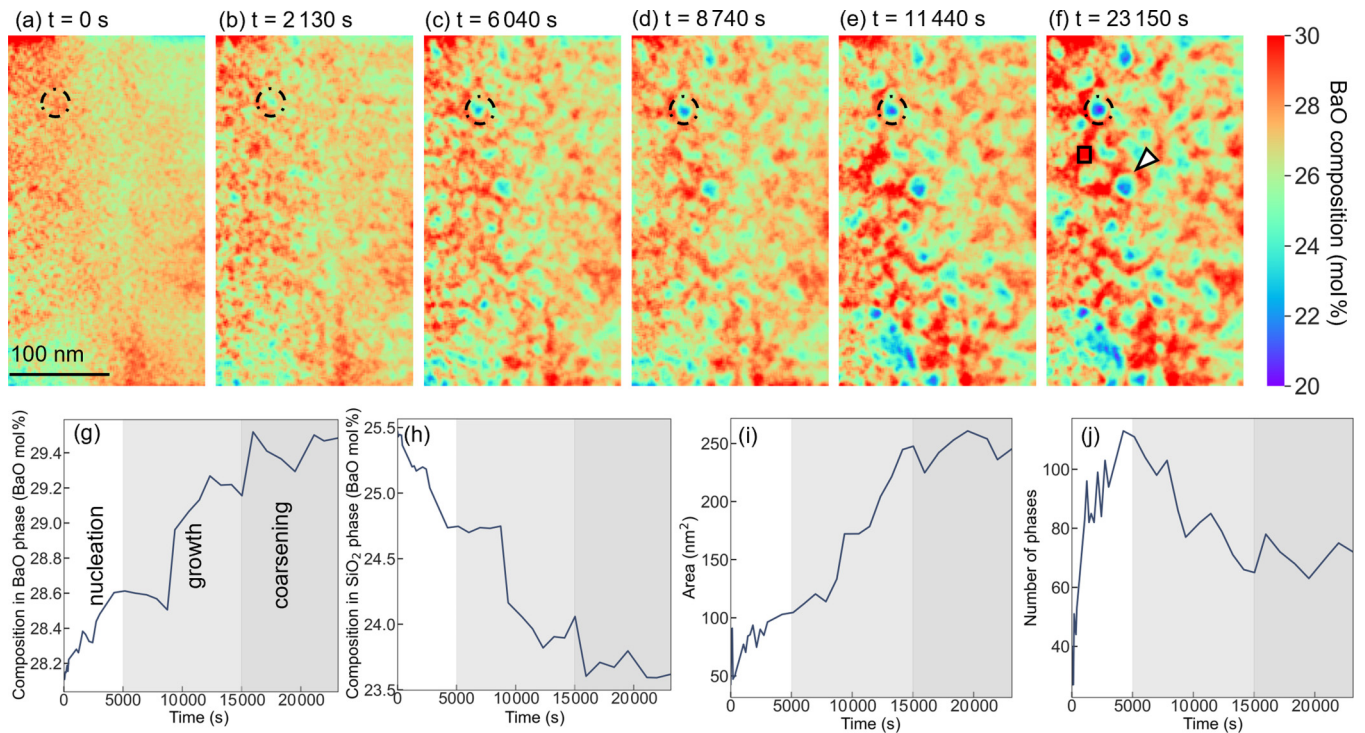


FIG. 2. Temporal change in the compositional distribution. These images show the distribution after heating for (a) 0 s, (b) 2130 s, (c) 6040 s, (d) 8740 s, (e) 11440 s, and (f) 23150 s. The blue and red regions correspond to the SiO<sub>2</sub> phases (low BaO composition) and BaO phases (high BaO composition), respectively. The volume fraction of the SiO<sub>2</sub> phase is low (minor) while that of the BaO phase is high (major). Temporal changes in the (g) average BaO composition of the BaO phases, (h) average BaO composition of the SiO<sub>2</sub> phases, (i) the average area of the SiO<sub>2</sub> phases, and (j) the number of SiO<sub>2</sub> phases. The white, light gray, and dark gray regions in these graphs indicate the nucleation stage (initial stage), growth stage (intermediate stage), and coarsening stage (final stage), respectively.

show the temporal changes in the average area and number of SiO<sub>2</sub> phases, respectively. The BaO composition in the SiO<sub>2</sub> phases decreased, while that in the BaO phases increased. Additionally, the average area of the SiO<sub>2</sub> phases increased from  $t = 0$  to  $t = 15000$  s, at which point it remained constant. Similarly, the number of SiO<sub>2</sub> phases increased between  $t = 300$  s and  $t = 5000$  s; however, the number decreased between  $t = 5000$  s and  $t = 15000$  s and remained constant.

Therefore, in accordance with previous research [1], the above changes can be summarized as follows: The region of  $t = 0$  to 5000 s is the nucleation stage [initial stage, the white area in Figs. 2(g)–2(j)],  $t = 5000$  to 15000 s is the growth stage [intermediate stage, the light gray area in Figs. 2(g)–2(j)], and  $t = 15000$  s and above is the coarsening stage [final stage, the dark gray area in Figs. 2(g)–2(j)]. The number of phases increases in the nucleation stage with a slight increase in the average area of the SiO<sub>2</sub> phases. Additionally, the decrease in the coarsening rate in the final stage is also consistent with that reported in a previous study [29].

Hereafter, we investigate the compositional change of the intermediate stage in real space. We took the difference by subtraction of two consecutive compositional maps to visualize the amount of compositional change over time. Figure 3 shows the compositional difference maps; the red and blue colors correspond to the increase and decrease in the BaO composition, respectively. Initially, regions with rapid compositional changes were not observed [Fig. 3(a)]. However, there was a region where the composition rapidly changed

in Fig. 3(b) [indicated by a white arrow at the bottom left area]. The position of this region was displaced with time [Fig. 3(c); the region moved from lower left to upper right], which was also observed in other images. The increase in the BaO composition of the BaO phase in the region was relatively stable at approximately +2.0–+3.0 BaO mol % in all the compositional differential images. While BaO composition of the BaO phase increased rapidly in the region, that of the SiO<sub>2</sub> phase decreased. This decrease is attributed to the increased volume of the SiO<sub>2</sub> phases (increase in the ratio of SiO<sub>2</sub> phase in the thickness direction). Moreover, Fig. 4(b) shows the measurement of the temporal change in the local area of an individual SiO<sub>2</sub> phase [indicated by a white arrow in Fig. 2(f)], which shows the rapid increment in the area of the SiO<sub>2</sub> phase when the region migrates.

Briefly, the phase separation rapidly proceeded in some defined regions and the region migrated from the bottom left to top right. Additionally, the compositional change in Fig. 4(a) confirms the rapid change in the BaO composition. Figure 4(a) also shows the temporal change in the average BaO composition within the black rectangle region of Fig. 2(f). The BaO composition rapidly increased by 2.0 BaO mol % during the migration of the region (10550–12330 s). However, the composition scarcely changed after this migration, as shown in Figs. 4(a) and 4(b). Therefore, this region serves as the boundary between the domains where the progress of the phase separation was delayed and advanced. This boundary migrates from the advanced domain to the delayed one

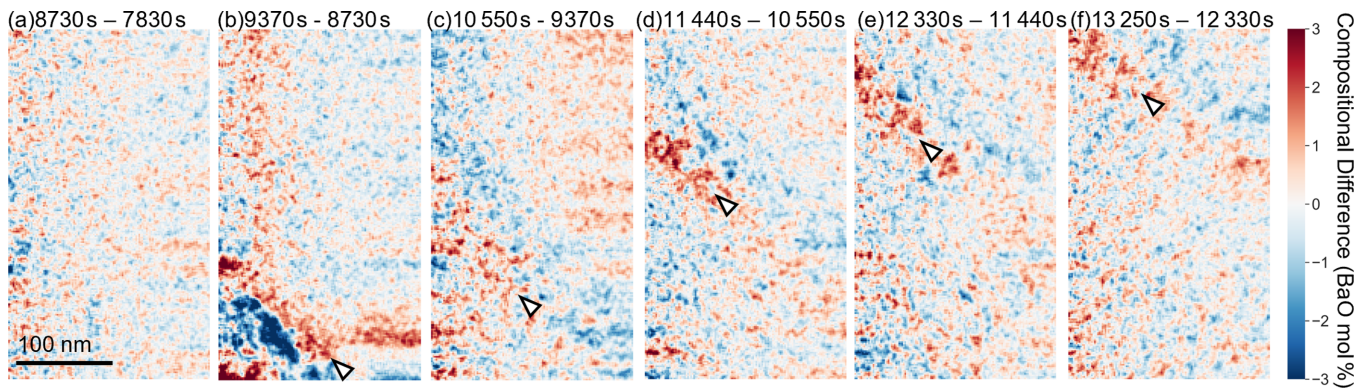


FIG. 3. Compositional difference between the two consecutive images. (a) 8730–7830 s, (b) 9370–8730 s, (c) 10550–9370 s, (d) 11440–10550, (e) 12330–11440 s, and (f) 13250–12330 s. The red and blue colors indicate the increase and decrease in the BaO composition, respectively. The depth of color corresponds to the amount of the increase/decrease of BaO composition. Arrows in the images from (b) to (f) indicate the regions where rapid change in the composition is observed.

at a speed of 0.039 nm/s. The boundary has a width of 38 nm [Fig. 3(d)], representing the region width where the phase separation progressed for 890 s, which corresponded to the interval of the sequential observation; thus, the actual boundary width was approximately 3.3 nm ( $38 - 0.039 \text{ nm/s} \times 890 \text{ s}$ ). Thus, the boundary with a compositional difference of 2.0 BaO % and a width of 3 nm migrates from the lower left to the upper right of the compositional maps. The reproducibility of domain formation and migration is confirmed as shown in Fig. S4 in the Supplemental Material [21]. We further verified the factors that influence the formation and movement of such boundaries by the phase-field simulations.

First, we employed the regular solution model for the Gibbs energy and considered the case where the microstructure domains with different degrees of the phase separation are connected. Figure 5(a) shows the relationship between the Gibbs energy and the composition. As shown in Fig. 5(b), we set the advanced and delayed domains on the lower left and upper right, respectively; the red and blue regions correspond to the BaO and SiO<sub>2</sub> phases, respectively. The temporal change in the phase-separated structure is shown in Figs. 5(b)–5(g). In this case, the downhill diffusion of both the elemental components occurred and the

compositional distribution at the domain boundary became smooth; the domain boundary did not move from the advanced domain (lower left) to the delayed domain (upper right). We then measured the temporal change in the composition near the boundary, as indicated by the black rectangle in Fig. 5(b). The result shown in Fig. 5(h) shows a gradual increase in the composition, which blurs the compositional difference at the domain boundary. Figures 5(i)–5(k) illustrate the temporal changes in the areas of the phases numbered P1, P2, and P3 of Fig. 5(b). P1 is the phase that the domain boundary has already passed at  $\tau = 0$ , P2 is the phase that the domain boundary is passing at  $\tau = 0$ , and P3 is the phase before the domain boundary passes through at  $\tau = 0$ . The area of P1 gradually decreased during the simulation, while that of P2 increased until  $\tau = 250$  and further became constant. In contrast, the P3 area continued to increase, while the increase rate decreased during the simulation. Moreover, the rapid increase in the area of the SiO<sub>2</sub> phase after the passage of the domain boundary was not observed in this simulation. Thus, employing the regular solution model for the Gibbs energy and joining the microstructure domains with different degrees of progress of phase separation did not reproduce the results of the *in situ* experiment, which are the migration of the domain boundary and the rapid increases of BaO composition in the BaO phase and the area of SiO<sub>2</sub> phases.

Next, we presume the multimetastability of the amorphous phase, which could originate from the short-range or medium-range order [30] at specific compositions in an amorphous solid. However, it is challenging to formulate the Gibbs energy with considering the structural order due to the insufficient precise knowledge about the structure of amorphous solids. Thus, we approximated the Gibbs energy using a polynomial function of only composition; the Gibbs energy is assumed to have several local minima at specific compositions. The polynomial function derived Gibbs energy model is just a toy model but is assumed to capture the essence of the multimetastability of the amorphous phase. Figure 6(a) shows the Gibbs energy provided by the polynomial function of composition with several numbered energy minima. The microstructure consisting of two phases with the compositions numbered 1 and 5 is the equilibrium state of the system. We placed the metastable two-phase microstructure domain

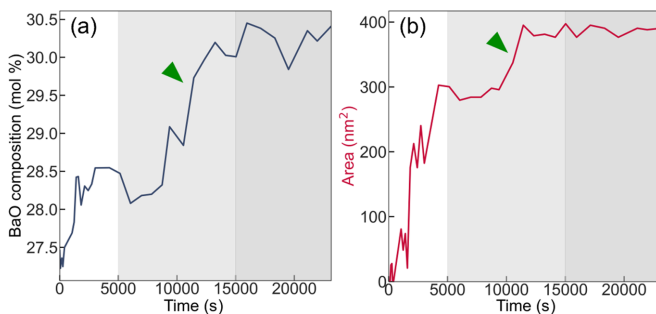


FIG. 4. Temporal change in (a) the average composition of the BaO phase measured from the region in the black rectangle [Fig. 2(f)] and (b) the area of the SiO<sub>2</sub> phase indicated by the white arrow [Fig. 2(f)]. Green arrows indicate the rapid increase in the composition and area during the region movement (10550–12330 s) where the phase separation rapidly proceeds. Both the composition and area slightly change after the movement of the region.

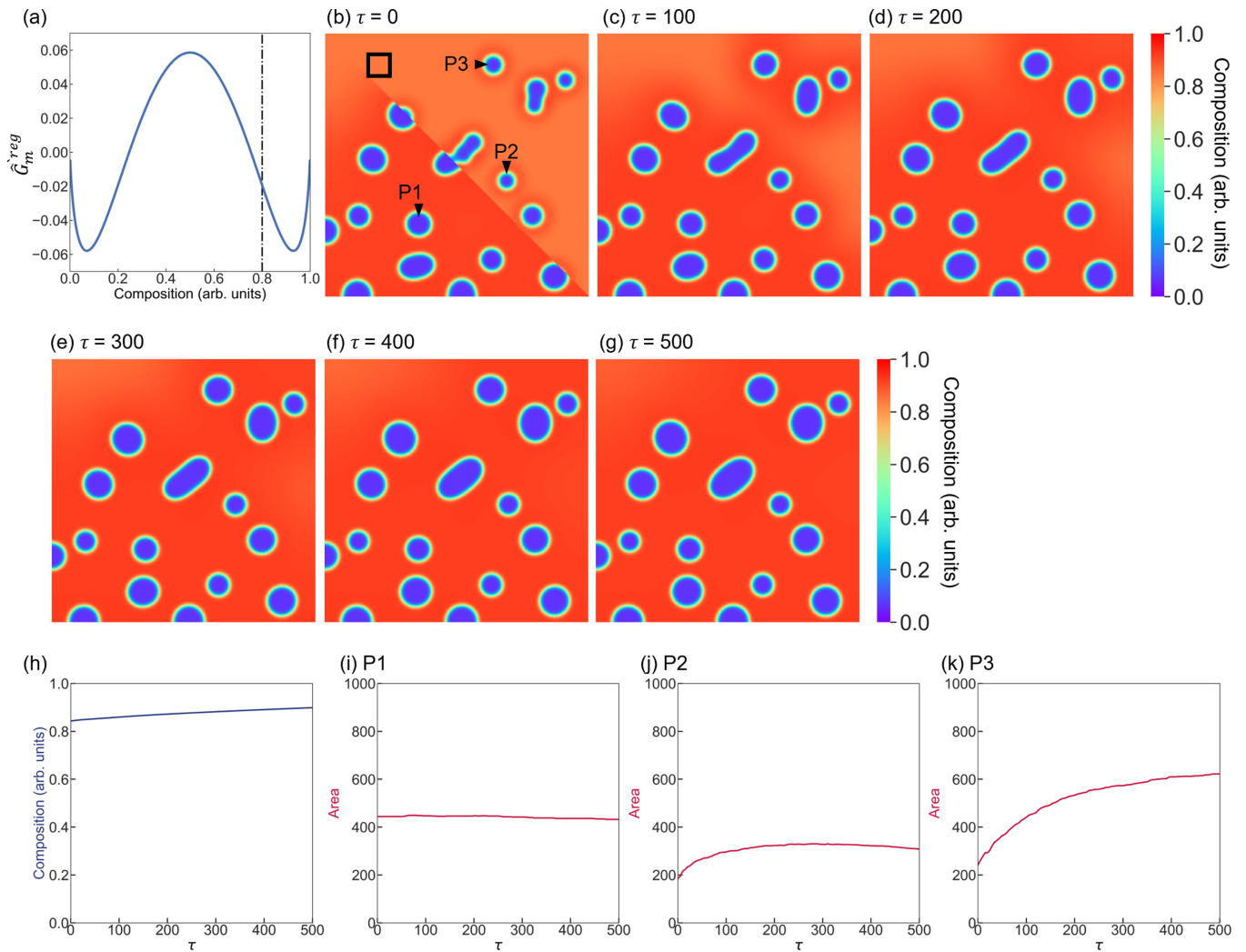


FIG. 5. (a) The Gibbs energy curve under the regular solution approximation. The vertical dash-dot line indicates the average composition. (b) The initial compositional distribution with a boundary between different degrees of phase separation progress (right top: delayed, left bottom: progressed). (b)–(g) Temporal changes in the compositional distribution. (h) Temporal change of the average composition of the matrix phase measured from the black rectangle in (b). Temporal change of the areas of phases (i) P1, (j) P2, and (k) P3.

consisting of phases with the compositions numbered 3 and 4 in the upper right and those numbered 2 and 5 in the lower left and simulated the subsequent microstructure evolution. The simulation results are presented in Figs. 6(b)–6(h). The minor blue and red matrix phases in this simulation corresponded to the  $\text{SiO}_2$  and BaO phases of the *in situ* experiment, respectively. Compared to the regular solution model, the domain boundary did not blur and moved from the low-energy domain to the high-energy domain (from the lower left to the upper right). Figure 6(i) shows the temporal change in the matrix phase composition, which rapidly changes as the domain boundary passes ( $\tau = 3200$ ). Furthermore, a rapid increase in the minor phase area during the passage of the domain boundary was observed. Figures 6(j)–6(l) illustrate the temporal changes in the areas of the phases numbered P4, P5, and P6 [Fig. 6(c)]. P4 is the phase passed by the domain boundary at  $\tau = 0$ , P5 is the phase the domain boundary is passing at  $\tau = 0$ , and P6 is the phase before the domain boundary passes through at  $\tau = 0$ . The area of P4 slightly increased, while the increase rate was constant during the simulation. However,

the area of P5 increased until  $\tau = 2000$  and further became constant. The time at which this increase halted coincided with the time at which the domain boundary passage was completed. A similar result was also observed in P6.

The simulations using the polynomial model for the Gibbs energy qualitatively reproduced the temporal changes observed in the *in situ* experiments, which are the migration of the domain boundary and the rapid increases in BaO composition in the BaO phase and the area of  $\text{SiO}_2$  phases. Thus, the experimentally observed characteristic changes in the phase-separated structure are attributable to the multi-metastability of the amorphous phase. It is worth noting that the phase transition occurs at the boundary between the low- and high-energy metastable microstructure domains, and the microstructure evolution progresses through the migration of the domain boundary, as observed in the *in situ* experiment.

The BaO composition in the BaO phases and area of the  $\text{SiO}_2$  phases rapidly increased during the phase transition at the domain boundary. After the phase transition, these changes in the composition and the area of  $\text{SiO}_2$  phases

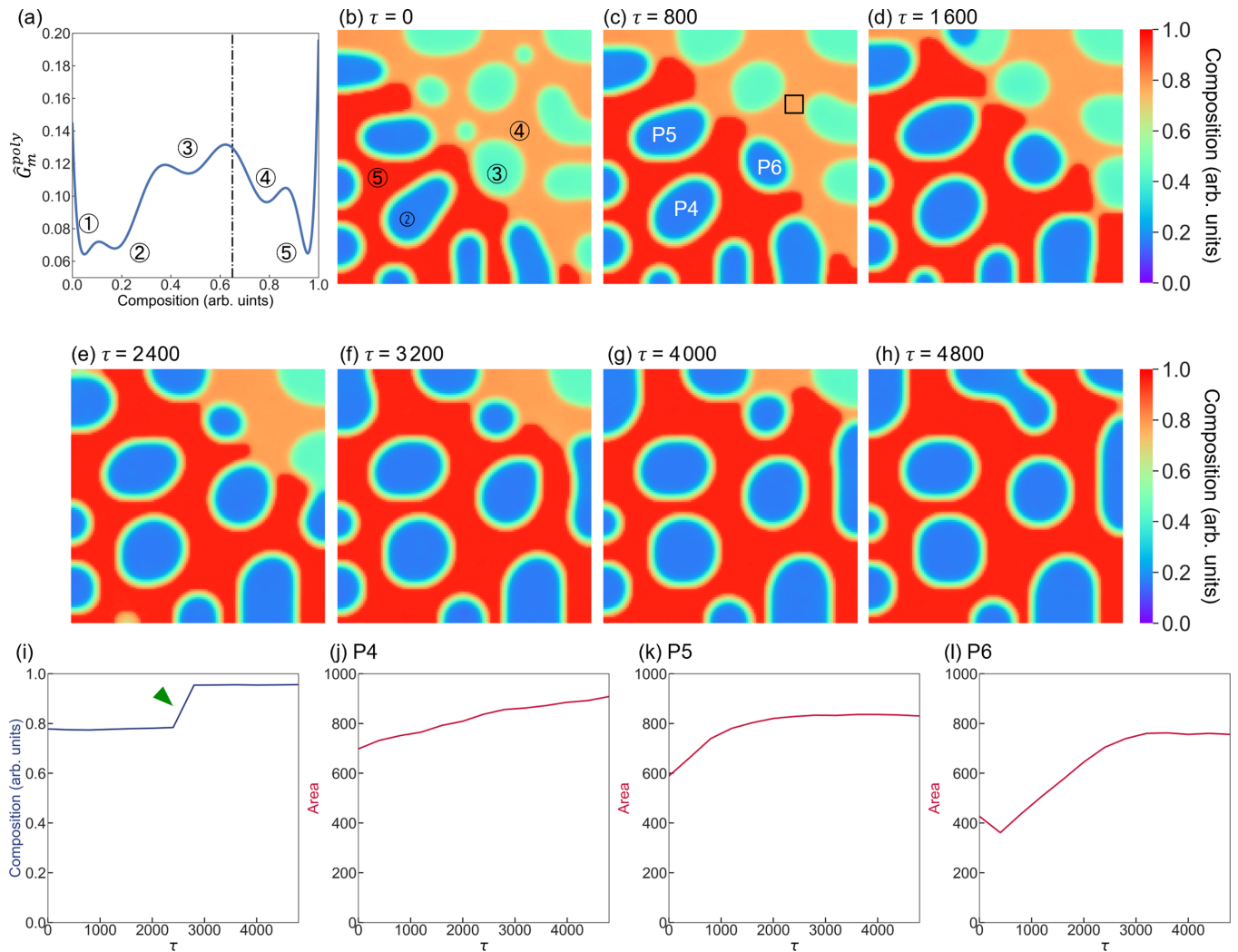


FIG. 6. (a) The Gibbs energy curve under the polynomial expression. There are five basins in the Gibbs free energy curve. Basins 2, 3, and 4 are the metastable states, and basins 1 and 5 are the most stable states. The vertical dash-dot line indicates the average composition. (b) The initial compositional distribution with a boundary between the different degrees of progress of phase separation (right top: delayed, left bottom: progressed). (b)–(h) Temporal change in the compositional distribution. (i) Temporal change in the average composition of the matrix phase measured from the black rectangle region in (c). Temporal changes in the areas of phases (j) P4, (k) P5, and (l) P6.

slowed and almost stopped in the *in situ* experiment. In the terminal process of phase separation, the separated amorphous phase could have been crystallized, which may have led to the cessation of the coarsening of the phase-separated structure [15,31]. However, the HAADF STEM observation cannot reveal such a structural transition behavior; hence, further experiments such as *in situ* observation of local diffractions with low dose are required.

#### IV. CONCLUSION

In this study, we visualized the temporal changes of the phase-separated structure during binodal phase separation in a silicate-based glass. The *in situ* heating STEM observations were performed to investigate the phase-separated structure in the intermediate stage. We determined a rapid local change in the phase-separated structures and the formation of regions with advanced and delayed degrees of phase separation. The boundaries of domains migrated from the advanced region to

the delayed region. The comparison with phase-field simulations concluded that the multimetastability of the amorphous phase causes the rapid local change in the phase-separated structure and the formation and growth of domains. Our *in situ* observation method can be applied to other glassy materials and will contribute to revealing the detailed phase separation process of an amorphous solid.

#### ACKNOWLEDGMENTS

This study was supported by the Ministry of Education, Culture, Sports, Science and Technology (MEXT) through Grants No. 17H06094, No. 19H00818, No. 19H05787, and No. 20J10498. The STEM observation was performed at the NIMS microstructural characterization platform as part of the “Nanotechnology Platform” of MEXT, Japan. The authors acknowledge Dr. Uesugi at NIMS for his support with the experiment.

- [1] P. F. James, Liquid-phase separation in glass-forming systems, *J. Mater. Sci.* **10**, 1802 (1975).
- [2] W. Haller, Chromatography on glass of controlled pore size, *Nature (London)* **206**, 693 (1965).
- [3] T. Hashimoto, J. Kumaki, and H. Kawai, Time-resolved light scattering studies on kinetics of phase separation and phase dissolution of polymer blends. 1. Kinetics of phase separation of a binary mixture of polystyrene and poly(vinyl methyl ether), *Macromolecules* **16**, 641 (1983).
- [4] D. Bouttes, E. Gouillart, E. Boller, D. Dalmas, and D. Vandembroucq, Fragmentation and Limits to Dynamical Scaling in Viscous Coarsening: An Interrupted *In Situ* X-Ray Tomographic Study, *Phys. Rev. Lett.* **112**, 245701 (2014).
- [5] D. Schwahn, S. Janssen, and T. Springer, Early state of spinodal decomposition studied with small angle neutron scattering in the blend deuteropolystyrene and polyvinylmethylether: A comparison with the Cahn-Hilliard-Cook theory, *J. Chem. Phys.* **97**, 8775 (1992).
- [6] K. Binder and D. Stauffer, Theory for the Slowing Down of the Relaxation and Spinodal Decomposition of Binary Mixtures, *Phys. Rev. Lett.* **33**, 1006 (1974).
- [7] J. W. Cahn, The later stages of spinodal decomposition and the beginnings of particle coarsening, *Acta Metall.* **14**, 1685 (1966).
- [8] J. W. Cahn, On spinodal decomposition, *Acta Metall.* **9**, 795 (1961).
- [9] J. W. Cahn, On spinodal decomposition in cubic crystals, *Acta Metall.* **10**, 179 (1962).
- [10] J. W. Cahn and J. E. Hilliard, Free energy of a nonuniform system. III. Nucleation in a two-component incompressible fluid, *J. Chem. Phys.* **31**, 688 (1959).
- [11] K. B. Rundman and J. E. Hilliard, Early stages of spinodal decomposition in an aluminum-zinc alloy, *Acta Metall.* **15**, 1025 (1967).
- [12] J. W. Cahn, Phase separation by spinodal decomposition in isotropic systems, *J. Chem. Phys.* **42**, 93 (1965).
- [13] M. H. Cohen and D. Turnbull, Metastability of amorphous structures, *Nature (London)* **203**, 964 (1964).
- [14] H. Hijiyama, T. Kishi, and A. Yasumori, Effect of phase separation on crystallization of glasses in the BaO-TiO<sub>2</sub>-SiO<sub>2</sub> system, *J. Ceram. Soc. Jpn.* **117**, 120 (2009).
- [15] P. D. Graham and A. J. McHugh, Kinetics of thermally induced phase separation in a crystallizable polymer solution, *Macromolecules* **31**, 2565 (1998).
- [16] D. Chen, Z. Wan, Y. Zhou, P. Huang, J. Zhong, M. Ding, W. Xiang, X. Liang, and Z. Ji, Bulk glass ceramics containing Yb<sup>3+</sup>/Er<sup>3+</sup>:  $\beta$ -NaGdF<sub>4</sub> nanocrystals: Phase-separation-controlled crystallization, optical spectroscopy and upconverted temperature sensing behavior, *J. Alloys Compd.* **638**, 21 (2015).
- [17] D. Zhou, A.-C. Shi, and P. Zhang, Numerical simulation of phase separation coupled with crystallization, *J. Chem. Phys.* **129**, 154901 (2008).
- [18] K. Nakazawa, S. Amma, and T. Mizoguchi, *In situ* observation of the dynamics in the middle stage of spinodal decomposition of a silicate glass via scanning transmission electron microscopy, *Acta Mater.* **200**, 720 (2020).
- [19] K. Nakazawa, T. Miyata, S. Amma, and T. Mizoguchi, Identification of nanometer-scale compositional fluctuations in silicate glass using electron microscopy and spectroscopy, *Scr. Mater.* **154**, 197 (2018).
- [20] J. E. Shelby, Effect of morphology on the properties of alkaline earth silicate glasses, *J. Appl. Phys.* **50**, 8010 (1979).
- [21] See Supplemental Material at <http://link.aps.org/supplemental/10.1103/PhysRevResearch.4.033052> for the detailed image processing and experimental results.
- [22] T. P. Seward III, D. R. Uhlmann, and D. Turnbull, Phase separation in the system BaO-SiO<sub>2</sub>, *J. Am. Ceram. Soc.* **51**, 278 (1968).
- [23] T. P. Seward III, D. R. Uhlmann, and D. Turnbull, Development of two-phase structure in glasses, with special reference to the system BaO-SiO<sub>2</sub>, *J. Am. Ceram. Soc.* **51**, 634 (1968).
- [24] A. Romero-Serrano, A. Cruz-Ramirez, B. Zeifert, M. Hallen-Lopez, and A. Hernandez-Ramirez, Thermodynamic modeling of the BaO-SiO<sub>2</sub> and SrO-SiO<sub>2</sub> binary melts, *Glass Phys. Chem.* **36**, 171 (2010).
- [25] Y. Gueguen, P. Houizot, F. Célaríe, M. Chen, A. Hirata, Y. Tan, M. Allix, S. Chenu, C. Roux-Langlois, and T. Rouxel, Structure and viscosity of phase-separated BaO-SiO<sub>2</sub> glasses, *J. Am. Ceram. Soc.* **100**, 1982 (2017).
- [26] C. Ophus, Four-dimensional scanning transmission electron microscopy (4D-STEM): From scanning nanodiffraction to ptychography and beyond, *Microsc. Microanal.* **25**, 563 (2019).
- [27] P. Petschek and H. Metiu, A computer simulation of the time-dependent Ginzburg-Landau model for spinodal decomposition, *J. Chem. Phys.* **79**, 3443 (1983).
- [28] K. Nakazawa, K. Mitsuishi, K. Shibata, S. Amma, and T. Mizoguchi, Local thickness and composition measurements from scanning convergent-beam electron diffraction of a binary non-crystalline material obtained by a pixelated detector, *Ultramicroscopy* **217**, 113077 (2020).
- [29] E. D. Siggia, Late stages of spinodal decomposition in binary mixtures, *Phys. Rev. A* **20**, 595 (1979).
- [30] A. P. Sokolov, A. Kisliuk, M. Soltwisch, and D. Quitmann, Medium-Range Order in Glasses: Comparison of Raman and Diffraction Measurements, *Phys. Rev. Lett.* **69**, 1540 (1992).
- [31] P. D. Graham, A. J. Pervan, and A. J. McHugh, The dynamics of thermal-induced phase separation in PMMA solutions, *Macromolecules* **30**, 1651 (1997).